McMillan Mitchell (Orcid ID: 0000-0002-8590-488X)

Schoenbohm Lindsay, M (Orcid ID: 0000-0001-7898-356X)

Large-scale Cenozoic Wind Erosion in the Puna Plateau: The Salina del Fraile Depression

Mitchell C. McMillan[1] and Lindsay M. Schoenbohm[1,2]

[1]Department of Earth Sciences, University of Toronto, Toronto, Ontario M5S 3B1, Canada

[2] Department of Chemical and Physical Sciences, University of Toronto Mississauga, Mississauga, Ontario L5L 1C6, Canada

Corresponding author: Mitchell McMillan (mitchell.mcmillan@mail.utoronto.ca)

Key Points:

- The Salina del Fraile depression in the arid Puna Plateau was excavated by wind over the last 17 to 8.2 Ma
- Cross-sections imply up to 2 km of erosion along fold hinges, with remnant km-scale ridges and mesas analogous to landforms on Mars
- Wind can generate and sustain high relief topography, even without significant fluvial or glacial incision

This article has been accepted for publication and undergone full peer review but has not been through the copyediting, typesetting, pagination and proofreading process which may lead to differences between this version and the Version of Record. Please cite this article as doi: 10.1029/2020JF005682

©2020 American Geophysical Union. All rights reserved.

Abstract

Wind erosion is integral to the evolution of arid landscapes on Earth and Mars, but the nature of long-term wind erosion of bedrock is poorly understood. Here we describe the Salina del Fraile (SdF) depression in the Puna Plateau of the Central Andes, NW Argentina, as a landform excavated by wind over several million years. New structural cross-sections and a compilation of chronostratigraphic ages rule out the hypothesis that the depression was created by transtensional tectonics. Dated remnant lacustrine and alluvial deposits in the floor of the depression constrain the rate and timing of erosion. Late Oligocene–Miocene compressional folding uplifted friable strata that were preferentially eroded, resulting in the high-relief (900 m) depression. Up to 1.95 km and an average of 1.05 km of strata were eroded during the last 8.2 to 17 Ma, at rates of 0.06 to 0.23 mm/yr. These rates are similar to long-term average wind erosion rates reported in other regions. Coarse-grained eolian megaripples, yardangs, and elongated ridges indicate ongoing eolian abrasion and deflation, aided by salt weathering, of the floor of the depression. Megaripple migration across stony lag surfaces exposes fresh bedrock to continued erosion. The SdF also contains kilometer-scale mesas and ridges that we interpret as erosional remnants. These landforms are similar to megayardangs and erosional topography identified on the lower flanks of Mount Sharp, Gale crater, Mars. In such hyperarid landscapes characterized by lithologic heterogeneities, high relief landforms can be generated and sustained by wind erosion, without significant fluvial or glacial incision.

Plain Language Summary

We investigated the origin of a large topographic depression in the arid Puna Plateau of the Central Andes, NW Argentina. Previous research interpreted the depression as formed by faulting, but we found that it is likely formed by wind erosion. While rivers and glaciers are usually responsible for erosion on Earth, there is no evidence for river or glacier action in the Salina del Fraile. Rather, much like the surface of Mars, wind was primarily responsible for forming the depression and surrounding landscape over several million years. We show that wind was able to excavate the depression because tectonic folding brought fine-grained rocks close to the surface, where they were exposed to strong winds and breakdown by salt weathering. Wind erosion was active for the last 8.2 to 17 million years, and, as evidenced by large dust storms originating from this region, is ongoing today. Wind is lowering the surface at an average rate of 0.06 to 0.23 mm/yr, similar to previous studies. The Salina del Fraile can help researchers understand the long-term effects of wind erosion on Earth and Mars.

1 Introduction

The degree to which eolian processes shape the landscape morphology of arid regions is a long-standing point of contention (Brock & Twidale, 2011; Goudie, 2012), albeit one renewed by the exploration of wind-dominated planetary surfaces and their terrestrial analogues (e.g., Xiao et al., 2017). Wind erosion may outpace fluvial incision of bedrock in hyperarid regions, and wind can enhance the erosion of favorably-oriented bedrock canyons (Perkins et al., 2015). On a regional scale, eolian deflation and abrasion can remove hundreds of meters of strata, potentially accelerating tectonic deformation (Kapp et al., 2011). Regional eolian deflation influences Earth's climate through dust emission and often results in the development of widespread desert pavements, which may drive faster surface winds through a wind-albedo-wind feedback (Pullen et al., 2018; Abell et al., 2020). Such research shows how wind erosion, although outpaced by fluvial and other processes in more humid regions, plays an integral role in parts of Earth's arid Cenozoic orogenic belts. On Mars, wind-driven retreat of bedrock scarps is responsible for relatively young surface exposure ages in Gale

©2020 American Geophysical Union. All rights reserved.

crater, offering potential locations for sampling well-preserved complex molecules (Farley et al., 2014). Identifying regions of active eolian erosion on Mars is important for exploring geologic units that may preserve signs of ancient life (Chojnacki et al., 2018). Studying the effects of wind erosion is therefore critical for understanding how tectonic processes interact with Earth's climate, and how the surfaces of wind-dominated planets evolve over geologic time scales. Both of these efforts, however, are hampered by a relatively poor understanding of large-magnitude eolian landforms generated over many millions of years on Earth.

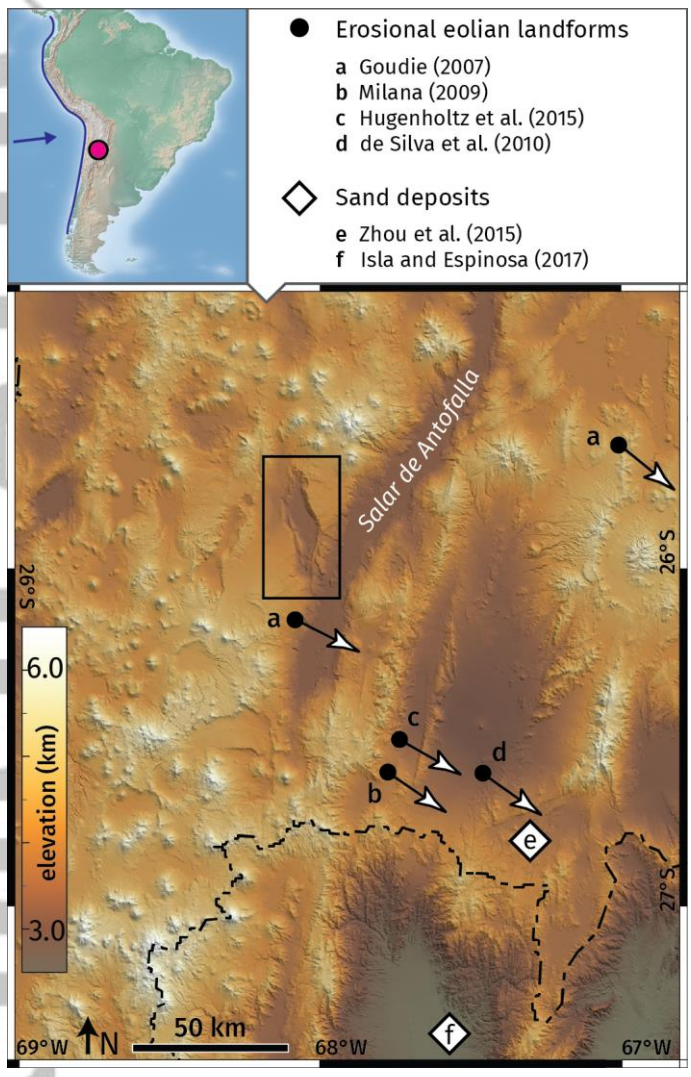

Figure 1. Digital surface model (DSM) of the southern Puna Plateau with study area boxed. Letters denote previous studies of eolian erosion (arrows) or deposition (diamonds), with arrows indicating wind direction. Inset shows study location and Nazca plate vector relative to South America. Dashed line shows limit of internally drained plateau. NASA SRTM DEM (1 arc second).

Here we show that the Salina del Fraile (SdF), a large, internally-drained depression in the southern Puna Plateau, NW Argentina, is an erosional landform excavated by wind over a time period of at least 8.2 Ma. We present new structural measurements and cross-sections that argue against tectonic lowering of the depression and instead imply up to 2 km of erosion where anticlinal folding exposed a thick package of friable, fine-grained strata. We describe remnants of alluvial surfaces within the depression to argue against significant

©2020 American Geophysical Union. All rights reserved.

fluvial incision during this time period. We also document eolian landforms over a wide range of spatial scales, both within and around the depression, to demonstrate the ubiquity of eolian erosion in this region. Finally, we use existing chronostratigraphic data to estimate the timing and rate of erosion and explore some implications of such long-term, large-scale wind erosion.

1.1 The Salina del Fraile

The Salina del Fraile (SdF) is an evaporite basin located to the west of the Salar de Antofalla in the southern Puna Plateau, NW Argentina (Figure 1). The present climate of the region is hyperarid, with mean annual rainfall of only ~14 mm (with a range of 0–70 mm) in the vicinity of the SdF (Bookhagen and Strecker, 2008). NASA MERRA reanalysis data indicate that the region experiences a cold desert climate, with summertime daily temperature highs of 20–25 °C and lows of -5–5 °C, and wintertime highs of 0–10 °C and lows of -10 to -15 °C, giving the region a cold desert climate (Figure S1). Aridity in this region began as early as the Eocene (Quade et al., 2015) and intensified during the Middle to Late Miocene, when the major evaporite playas such as the Salar de Antofalla began forming (Alonso et al., 1991; Strecker et al., 2007). Arid climates, in addition to suppressing fluvial processes, enhance eolian deflation and abrasion due to sediment desiccation, salt weathering, and reduced vegetation cover (e.g. Goudie, 2018).

Eolian deflation commonly occurs on the margins of evaporite playas, such as the SdF, because salt accumulation rapidly disintegrates bedrock and alluvial deposits and provides fine-grained particles for removal by wind (Goudie & Day, 1980). Salt accumulation in closed depressions therefore tends to reinforce further eolian excavation in a positive feedback, especially if the host lithology is susceptible to salt weathering, such as would be for porous sandstones or fine-grained siliciclastics (Goudie & Wells, 1995). Eolian deflation aided by salt weathering can lead to the formation of large depressions, as has been suggested for the Qattara Depression in Egypt (Aref et al., 2002). Eolian processes also interact with fluvial and lacustrine deposits in arid playas because precipitation events result in fine-grained sediment being transported and deposited on surfaces prone to deflation (Goudie, 2018).

The SdF is situated within a continental-scale NNW–SSE eolian system, in a region characterized by erosional landforms such as yardangs, megayardangs, and periodic bedrock ridges (Figure 1 and references therein). Significant eolian sand deposits are rare in the vicinity of the SdF, but occur further downwind in the SE Puna, in the Fiambalá basin (Figure 1), and in a belt stretching several hundred kilometers further SE (Isla & Espinosa, 2017). Strong winds in the region are associated with synoptic polar fronts that typically occur during a windy season that lasts from May to October (Milana & Kröhling, 2017). Major dust storms have been imaged originating from evaporite playas on the Puna Plateau, including from the SdF (Goudie & Wells, 1995; Milana & Kröhling, 2017). Although the Puna Plateau is internally drained, sediment is removed from the southern Puna by wind, potentially providing a source of the Chaco-Pampean loess deposits in eastern Argentina (Milana & Kröhling, 2017) and dust in Eastern Antarctic ice cores (e.g., Gaeiro, 2007).

The SdF-Antofalla region was tectonically deformed as it was incorporated into the Andean orogenic wedge ~30–20 Ma, uplifting and deforming a Paleogene foreland basin system (Carrapa et al., 2005; Kraemer et al., 1999; Zhou et al., 2017). Cenozoic units outcropping in the SdF consist of the Paleogene Quiñoas and Chacras Formations, a coarsening-upward sequence of continental siliciclastics; the Neogene Potrero Grande

©2020 American Geophysical Union. All rights reserved.

Formation, a volcaniclastic unit with interbedded ashes and ignimbrites; and later volcanic flows and ignimbrites (Kraemer et al., 1999). The Quiñoas Formation unconformably overlies pre-Cenozoic rocks. In the study area, pre-Cenozoic rocks consist of Permian to Jurassic sedimentary and volcanic strata exposed in the northern part of the SdF depression (Voss, 2002). An angular unconformity separates the Potrero Grande Formation from underlying units, which are tilted to the SE.

The SdF is a rhomboidal topographic depression, 300 km^2 in area, with up to 900 m of topographic relief. Goudie and Wells (1995) hypothesized that the SdF (therein termed Potrerillos Depression) is analogous to a giant deflation pan, "the largest Altiplano basin of primarily aeolian origin" (pg. 22), but later research in the region diverged from this interpretation (Figure 2). The depression's conspicuous planform shape, rectilinear slopes, and what appeared to be rotated fault blocks along the western edge (labelled "elongated ridges" in Figure 3), led some to interpret it as a pull-apart basin, with the basin floor lowered by major normal faults as a result of a left step in an inferred N–S-trending left-lateral fault system (Reijs & McClay, 2003; Voss, 2002). Others mapped the depression as the core of an anticline with only minor faults, an interpretation that also satisfies chronostratigraphic constraints (Adelmann, 2001; Kraemer et al., 1999; Seggiaro et al., 2007). The structural interpretation of the SdF is critical, because a compressional origin requires the erosion of material in order to create a morphologic depression, while a pull-apart basin would not necessitate erosion (Figure 2).

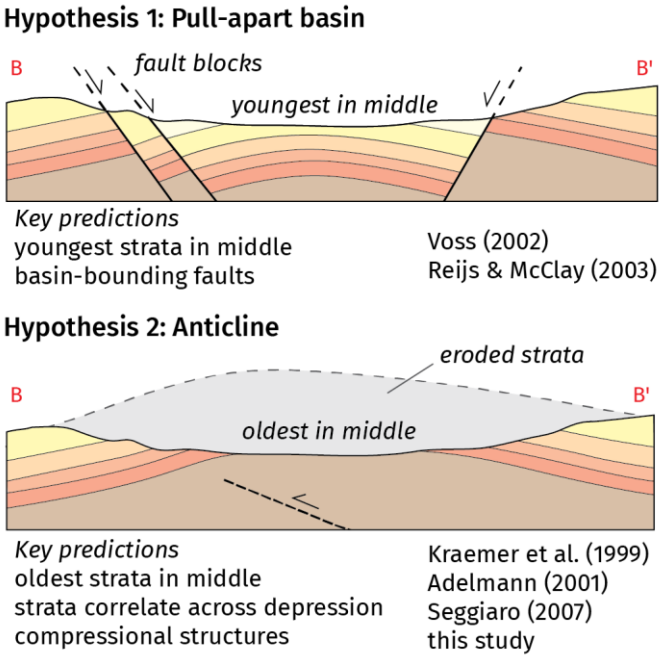

Figure 2. Theoretical cross-sections illustrating the two competing hypotheses for the structural setting of the Salina del Fraile depression. Strata are drawn schematically along topographic section B-B' (Figure 3).

2 Materials and Methods

We collected measurements of bedding planes in the field using a Brunton Transit (n=40) and mapped the Cenozoic geology along two transects spanning the depression (profiles A and B in Figure 3). Transects were oriented perpendicular to major structures, allowing us to test the two hypotheses for the formation of the depression (pull-apart basin or compressional folding). To supplement our structural data, we also digitized strikes and dips

©2020 American Geophysical Union. All rights reserved.

from Voss (2002, n=52) and Reijs and McClay (2003, n=39) within the Salina del Fraile by georeferencing their maps in a GIS environment. Our field measurements closely agree with nearby data from these sources. Cross-sections were constructed using the kink-band method; because a main objective is to estimate the magnitude of erosion, cross-sections were drawn to minimize the amount of eroded material, within realistic geologic constraints.

Chronostratigraphic data were compiled from Adelmann (2001, n=29), Canavan et al. (2014, n=14) and Quade et al. (2015, n=11) and mapped when sample locations were given. For ages referenced to a stratigraphic column, we mapped the locations of the samples onto cross-section B-B' using their stratigraphic positions. These data consist of single grain Ar–Ar (n=16; biotite, plagioclase, potassium feldspar), K–Ar (n=12; feldspar, biotite, glass) and U–Pb (n=21, zircon) ages and a K–Ar whole rock age (n=1, andesite). Dated lithologies were largely volcanic tuff (n=38), followed by ignimbrite (n=5), andesite (n=2) and other volcanic lithologies (n=5). The data tabulated by Adelmann (2001, Appendix 1 therein) were published in part by Kraemer et al. (1999, Table 1 therein) and the analytic methods were described by Voss (2002, Table 1 therein). Ar–Ar age determinations were performed by the GEOMAR Forschungszentrum (Kiel, Germany) and K–Ar age determinations by GEOCHRON Laboratories, Krueger Enterprises, Inc. (Cambridge, Massachusetts). U–Pb ages of volcanic zircons were published by Canavan et al. (2014, Tables DR1 and DR2 therein) and Quade et. al (2015, Table 4 therein) and were determined by laser ablation multicollector inductively coupled plasma mass spectrometry (LA-MC-ICPMS) at the University of Arizona LaserChron Center. All ages compiled here are reported with 2σ uncertainty.Structural and chronostratigraphic data used here are available in the University of Toronto Dataverse (McMillan and Schoenbohm, 2020).

Predominant strong wind directions were inferred from landforms mapped using high resolution aerial imagery obtained from Bing Maps (~30 cm/px; Figure S2). Landforms include yardangs, megaripples, dust streaks, and abraded bedrock surfaces. We assume prevailing wind directions are well represented by the long axes of yardangs that taper downwind (n=21); by directions normal to the average crestline orientation of asymmetric megaripples, with more gentle stoss slopes and steeper lee slopes (n=5); and by light-toned dust streaks extending downwind from evaporite or alluvial playas (n=4). Each landform yielded a single measurement of wind direction. Where fields of periodic yardangs or megaripples occur, the wind directions mapped in Figure 3 represent an average of all measurements for the field. Although aerial imagery alone did not permit us to unambiguously distinguish the stoss and lee slopes of megaripples, their orientations and associated wind directions were verified in the field. Abraded bedrock surfaces displaying elongated ridges and grooves may also provide information about wind directions; although we are less confident about these measurements (n=2), they parallel other landforms and are therefore shown as dashed arrows in Figure 3. Following Perkins et al. (2019), regional wind and temperature data were obtained from the NASA MERRA reanalysis dataset (https://disc.gsfc.nasa.gov/) for a period spanning the windy seasons (May to October) of the years 1982–1992. This decade, the earliest in the dataset, was chosen to minimize any effects of anthropogenic climate change. Hourly wind speeds and downwind directions at a height of 2 m are plotted in the inset of Figure 3. Daily statistics for surface temperatures at a height of 2 m are plotted in Figure S1.

We mapped alluvial surfaces and terrace remnants in the depression using the ALOS World 3D (1 arc second) DSM provided by JAXA and verified these interpretations with field observation. The depths of internally drained portions of the landscape were analyzed using TopoToolbox (Schwanghart & Scherler, 2014).

©2020 American Geophysical Union. All rights reserved.

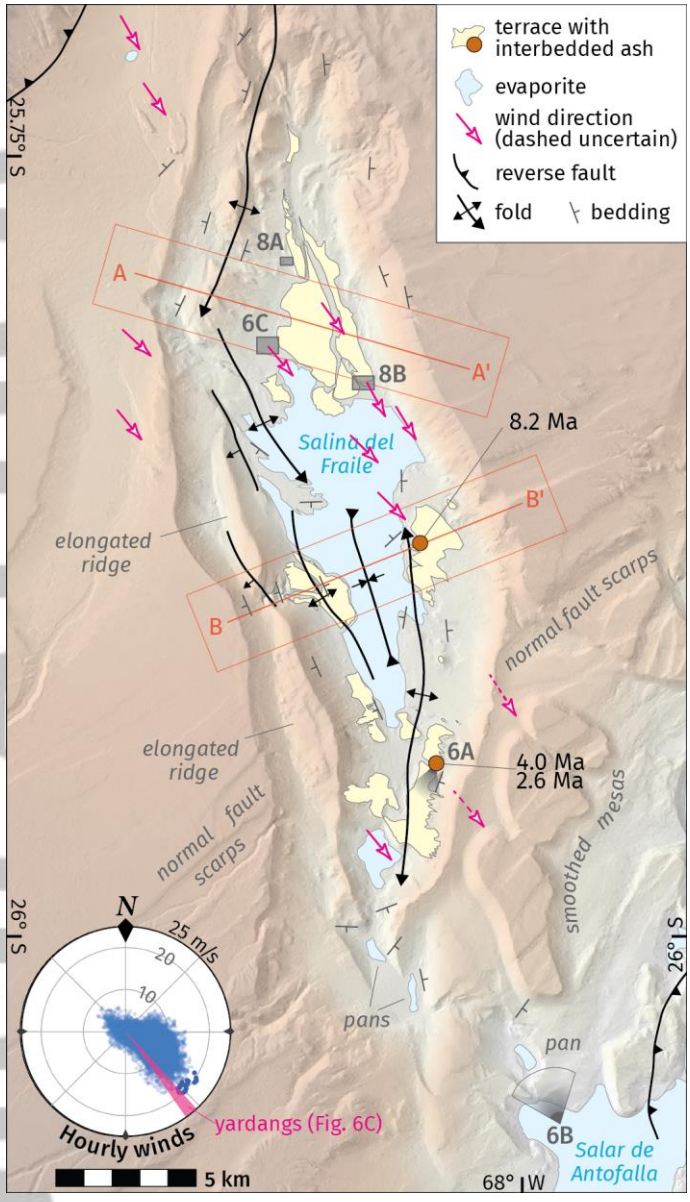

Figure 3. Topographic hillshade of the Salina del Fraile. Red boxes denote cross-sections in Figures 4 and 5. Lettered symbols denote images in Figures 6 and 8. Strikes and dips selected from our data, Voss (2002), and Reijs and McClay (2003). Dated ashes and their locations are from Adelmann (2001). Inset plots regional wind speeds and downwind directions from NASA MERRA hourly reanalysis data (https://disc.gsfc.nasa.gov/) during the windy seasons of 1982–1992, with winds >18 m/s shown as bold dots. Pink segment shows orientations of yardangs mapped in Figure 8c.

3 Results and Discussion

3.1 Structural interpretation: Against extensional lowering of the depression

Strata are deformed by a series of roughly N–S-trending folds, with no basin-bounding normal faults (Figure 3). The northern portion of the SdF consists of a roughly N–S trending, southward plunging anticline that exhumes Permian and Jurassic strata (Figure 4). The fold axial plane dips to the east, and the Potrero Grande thickens rapidly, with dips

©2020 American Geophysical Union. All rights reserved.

decreasing up-section on the western limb, consistent with syntectonic sedimentation (Figure 4). On the eastern limb of the fold, late Paleogene strata are truncated by the unconformity at the base of the Potrero Grande Formation. Chronostratigraphic data confirm that the flat interior of the depression here is composed of the lower member of the Quiñoas Formation, with K–Ar ages of 37.6 Ma of a volcanic tuff and 36.7 Ma on a reworked pumice clast (Adelmann, 2001). This interpretation is supported by U–Pb zircon ages from Canavan et al. (2014), who dated six volcanic tuffs outcropping in the eastern wall of the depression, 3.5 km north of Section A-A', with ages ranging from 36.1 Ma to 34.4 Ma.

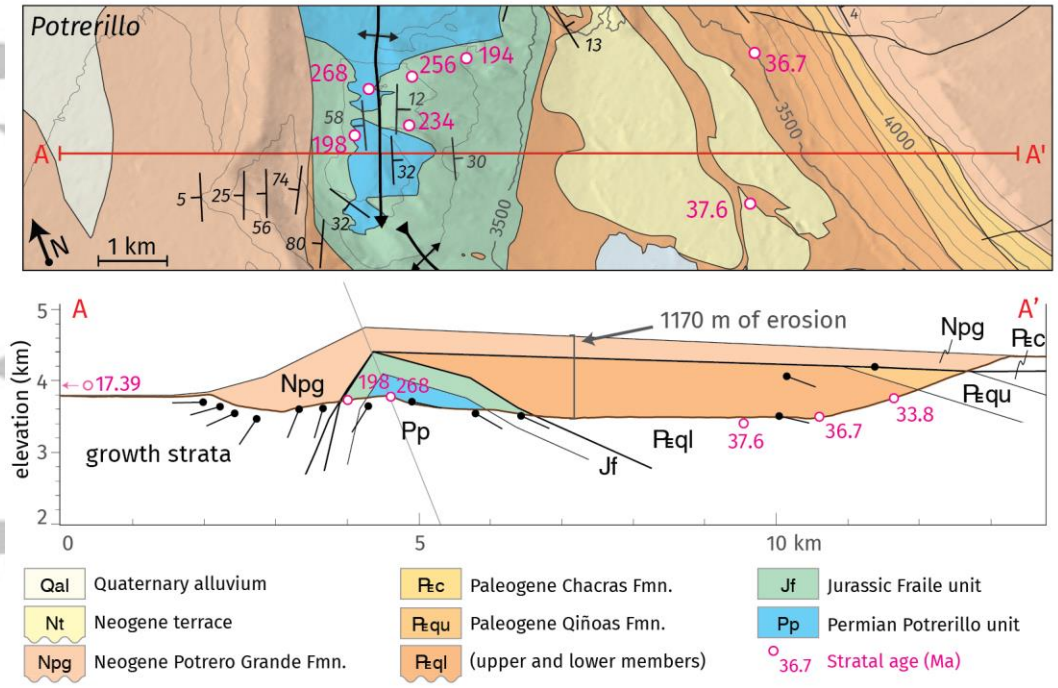

Figure 4. Section A-A'. Geologic strip-map and structural cross-section of the northern Salina del Fraile near Potrerillos. Chronostratigraphic ages compiled from Adelmann (2001), Canavan et al. (2014), and Quade et al. (2015). Strikes/dips measured in the field supplemented with those from Voss (2002) and Reijs and McClay (2003) as dark gray symbols.

The central portion of the SdF consists of a series of gentle anticlines separated by a doubly inward-plunging syncline (Figure 5). Small kink-band folds mapped as monoclines are present on the western limb of the westernmost anticline, where strata are locally overturned. The Vega Chacras canyon on the western limb of this anticline is well-studied, with a chronostratigraphic record comprised of 17 ages in a transect across what had been interpreted as rotated fault blocks (Adelmann, 2001; Canavan et al. 2014; Quade et al., 2015). Stratal ages range from 18.0 Ma at the top of the canyon (K–Ar of volcanic glass) to 38.5 Ma near its base (U–Pb of volcanic zircon). These ages are consistent with uplifted, west-dipping, Cenozoic strata on the western limb of an anticline (Figure 5), rather than a late Miocene normal-fault growth sequence (Reijs and McClay, 2003). We found no field evidence for repetition of strata in this location, and stratal ages show no offsets across what had been interpreted as normal fault blocks (Figure 5).

©2020 American Geophysical Union. All rights reserved.

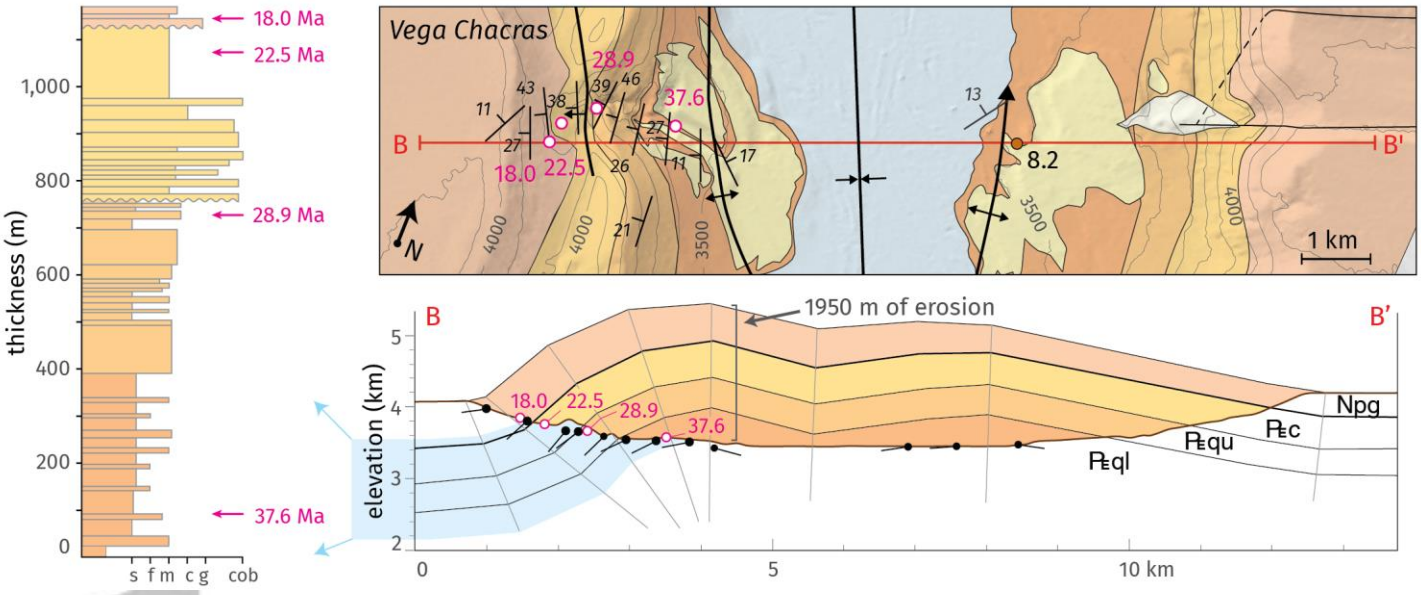

Figure 5. Section B-B'. Geologic strip-map and structural cross-section of the central Salina del Fraile near Vega Chacras. Chronostratigraphic ages selected from Adelmann (2001), Canavan et al. (2014), and Quade et al. (2015). Strikes/dips measured in the field supplemented with those from Voss (2002) and Reijs and McClay (2003) as dark gray symbols. Stratigraphic column redrawn from Adelmann (2001). Refer to Figure 4 for legend.

The relative age of strata in the floor of the depression is a key prediction of both hypotheses (Figure 2). Strata outcropping throughout the floor of the depression have been dated by multiple studies. Quade et al. (2015) obtained an age of 38.5 ± 0.7 Ma from an interbedded tuff near the base of Vega Chacras canyon, while Canavan et al. (2014) obtained ages of 35.7 ± 0.9 Ma and 33.9 ± 0.9 Ma from an outcrop in the southern portion of the depression. Adelmann (2001) obtained ages of 37.6 ± 0.3 Ma and 36.7 ± 0.3 Ma from bedrock exposures in the floor of the northern part of the depression. These studies indicate that the floor of the depression is composed of relatively old bedrock, the Lower Member of the Quiñoas Formation (late Eocene to early Oligocene). The lithology of this unit consists playa mudstones, evaporites, siltstones, and sandstones (Kraemer et al., 1999) up to 2 km thick in the Salina del Fraile (Figure 4). Although the depression does contain thin Neogene terrace deposits (Figures 4 and 5, see below), these deposits rest in angular unconformity on older units and are not consistent with structural lowering of the depression. It is possible that smaller extensional structures are hidden beneath the modern evaporite playa, but exposures of the Quiñoas Formation would necessarily limit any such structures to a small area, and they would not be capable of explaining the origin of the depression.

These observations indicate a purely contractional structural setting for the SdF, rather than an extensional or transtensional one (Hypothesis 2, Figure 2). The eastern dip of fold axial planes is consistent with fault propagation folding, possibly due to blind, west-vergent thrust faults associated with a major reverse fault system to the east (Adelmann, 2001; Voss, 2002; Seggiaro et al., 2007). The two main N-S trending anticlines in the NW and SE parts of the study area have a wavelength of ~15 km and their geometry mirrors the rhomboidal planform geometry of the depression (Figure 3). Compressional folding and subsequent erosion thus provide a compelling explanation for the geometry of the depression.

©2020 American Geophysical Union. All rights reserved.

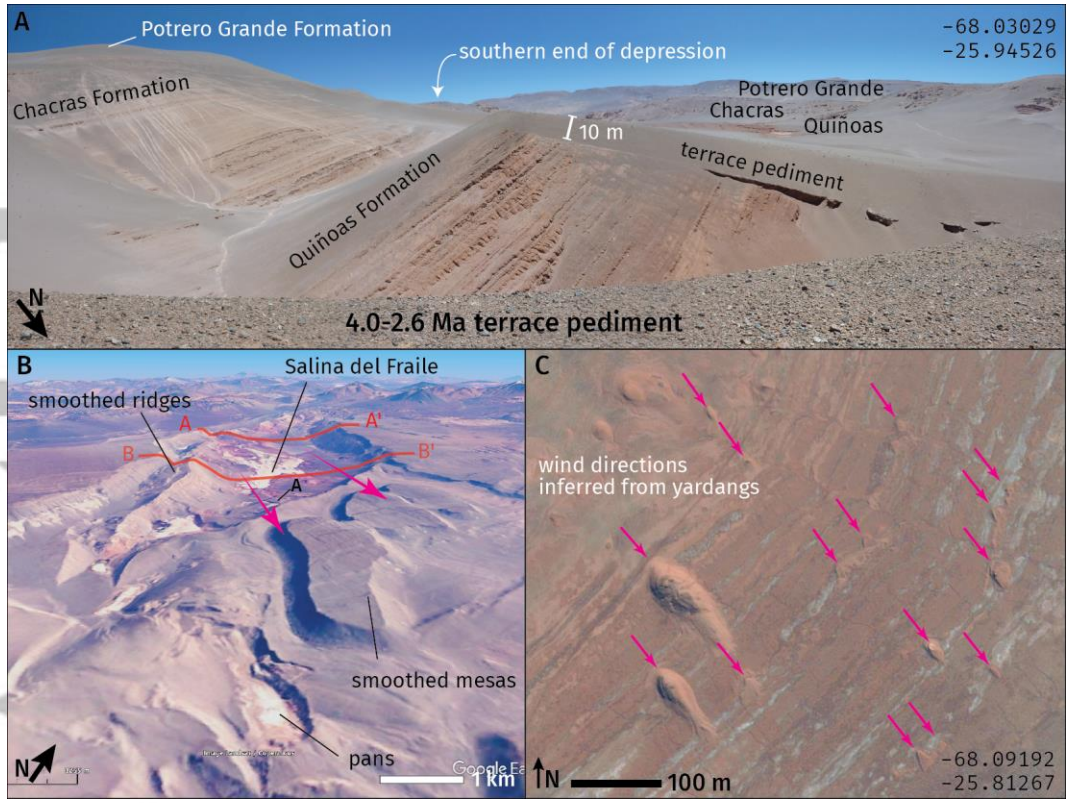

Figure 6. Geomorphological evidence of wind erosion across spatial scales. (**a**) Unconformity between 2.6–4.0 Ma terrace deposit and Cenozoic units, showing erosional streamlining of terrace edge. (**b**) Upwind view of the Salina del Fraile (Google Earth). Location of Figure 6a labelled A. (**c**) Yardangs carved into the friable Paleogene Quiñoas Formation. Aerial imagery from Bing Maps. Refer to Figure 3 for the locations of images.

3.2 Little evidence for fluvial incision

If the SdF depression is not formed by structural lowering of the basin floor, then it must have been carved by erosive processes. We rule out the possibility of glacial erosion in this hyper-arid region because no glacial or paleoglacial landforms are present in the Salar de Antofalla region (Haselton et al., 2002). We therefore examine the relative roles of fluvial and wind erosion. There is evidence of minor fluvial reworking within the depression. For example, several terraces cut into tilted Paleogene strata are present within the depression and capped by deposits 10–120 m thick (Figure 3). The terrace deposits (lacustrine and alluvial strata with gypsum-rich soil horizons) overlie tilted Paleogene bedrock in angular unconformity (Figure 6a) and were deposited in an existing topographic low (Voss, 2002). The terraces have been partially eroded, and their remnants now stand in relief above the SdF floor, often as yardangs (Figure S3b). Interbedded ashes in the terrace deposits dated to 2.6, 4.0, and 8.2 Ma (Adelmann, 2001) imply that significant erosion of the SdF occurred both before 8.2 Ma (to create the initial depression) and since 2.6 Ma (to erode the terraces and further deepen the depression). Erosional episodes were evidently punctuated by periods of net deposition or soil development.

The depression is not presently part of an integrated fluvial network. Making the highly conservative assumption that the depression was originally a fluvial valley and that wind erosion is only responsible for the portion of the internally drained topography provides

©2020 American Geophysical Union. All rights reserved.

an estimate of the minimum amount of wind erosion. The lowest point on the southern margin of the depression is blocked by an escarpment that extends >212 m above local base level and does not appear to have been uplifted structurally (Figure 7). Wind, which is capable of excavating internally drained depressions, is thus interpreted to be responsible for a minimum of 212 m of erosion (Figure 7). However, we find it unlikely that the depression was a fluvial valley in the past and argue for a larger magnitude of wind erosion. If the depression had been externally drained when the internal Neogene terraces were deposited, they would decrease in elevation to the south (i.e., downstream); in contrast, they decrease in elevation to the north, toward the center of the depression. Terrace deposit facies are also indicative of deposition in an internally drained basin in an arid climatic regime similar to the present. Finally, late Miocene–Pliocene units ouctropping on the eastern border of the Salar de Antofalla are sourced from, and thicken toward, the Sierra de Calalaste to the east, rather than the Salina del Fraile to the west (Adelmann, 2001). It is therefore unlikely that the SdF was drained fluvially during the last 8.2 Ma (the oldest dated ash in a terrace deposit).

While we argue that wind was responsible for excavating the internally drained depression, we do not discount the importance of fluvial processes for redistributing sediment within the SdF. Fluvial canyons and gorges are incised into bedrock along the margins of the SdF, most notably at Vega Chacras, Potrerillo, and Potrero Grande (Figure S2). These channels have headwaters in grassy marshes and are fed by groundwater seepage and possibly by overland flow during rare precipitation events. The drainage network around Potrero Grande, in particular, is responsible for significant alluvial and fluvial deposits in the NE part of the depression. In the southeastern corner of the depression, small rills and gullies incise gravelly surfaces capping bedrock terraces (Figure S3b). Although fluvial erosion is capable of widening a closed depression, eolian entrainment of the resulting deposits is required to increase its depth, as rivers cannot erode below the base level set by their outlet. Fluvial processes are likely important for detaching sediment and transporting it to the floor of the depression, where clasts are vulnerable to salt weathering and particles can be entrained by wind. Eolian entrainment of fluvial deposits also provides a source of abrasive sand for eroding bedrock surfaces downwind. As is clear from the bedrock terraces described above, deflation of material from the basin has outpaced deposition, resulting in deepening of the depression over time. The lacustrine, alluvial, and fluvial deposits capping terraces indicate that excavation of the SdF was episodic and punctuated by periods of net deposition. These episodes were likely driven by changes in climate, as has been suggested for internal terraces in depression in the Negev Desert, Israel (Plakht et al., 2000).

Accepted Article

©2020 American Geophysical Union. All rights reserved.

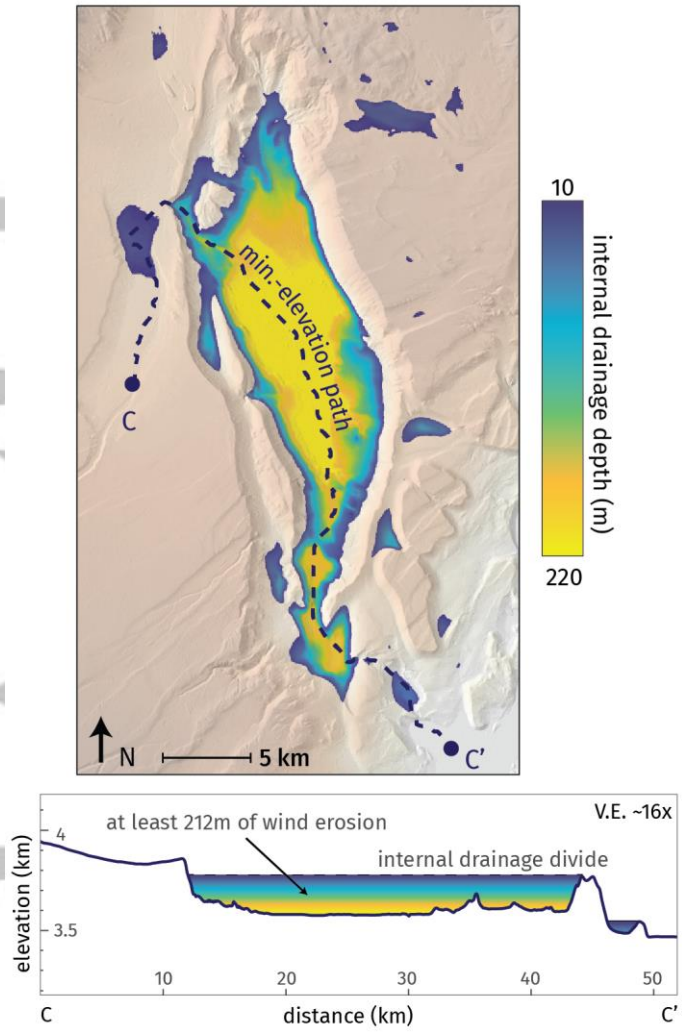

Figure 7. Internal drainage of the Salina del Fraile. The internal drainage depth approximates the minimum amount of wind (versus fluvial) erosion required to generate the observed topography. The transect follows the lowest-elevation path to the Salar de Antofalla. Internal drainage depth calculated using "fillsinks" function of TopoToolbox; transect calculated by routing flow using the "carve" preprocessor, which chooses the lowest elevation path across topographic highs (Schwanghart & Scherler, 2014).

3.3 Evidence in favor of wind erosion

Rather than extensional tectonics or fluvial erosion, we argue that wind is primarily responsible for forming the depression. There is abundant evidence for both eolian abrasion and deflation within and around the SdF (Figure S2; Goudie and Wells, 1995). Yardangs 10–100 m in length with ~1–5 m of relief are carved into lower Quiñoas Formation where it dips gently parallel to the wind direction (Figure 6c). Yardangs are streamlined eolian erosional landforms whose size and shape are controlled by the bedding orientation and heterogeneity of host strata (de Silva et al., 2010; Pelletier et al., 2018) as well as lithology. Five kilometers south of the yardangs, the Quiñoas Formation dips perpendicular to wind direction and outcrops as rough, sharp-crested hogbacks and smooth elongated ridges with length/width aspect ratios up to ~13 (Figure S4c). These ridges occur over a larger area than do the

©2020 American Geophysical Union. All rights reserved.

yardangs and also indicate the action of eolian abrasion and deflation scouring the basin floor.

Eolian megaripples are locally present with wavelengths of 1–3 m and heights of 10–20 cm (Figure 8; Figure S4a). The origin of coarse-grained megaripples is debated along with their classification as migrating (Milana, 2009; Hugenholtz et al., 2015) or static bedforms (de Silva, 2010; de Silva et al. 2013; Bridges et a., 2015). Observations of the internal structures and morphology of megaripples are broadly consistent with their downwind migration driven by saltation-induced creep (Lämmel et al., 2018). Aerial imagery reveals extensive fields of megaripples that developed on subhorizontal surfaces capped by conglomeratic deposits (Figure 8b). The planforms of these megaripples show evidence of migration similar to that observed by Hugenholtz et al. (2015), with orientations indicating NNW wind directions, consistent with other eolian landforms (Figure 3). The megaripples observed in the SdF thus give additional evidence of strong winds and the presence of abrasive, saltating particles that drive their downwind migration. Their downwind migration also exposes fresh bedrock (orange surfaces visible in Figure 8), providing a means for disrupting stony lag deposits that would otherwise protect bedrock against further erosion (Abell et al., 2020). Stony deposits are also disrupted by small gullies and rills that expose bedrock surfaces in the SE part of the depression (Figure S3b).

The sides of the depression are prominent rectilinear bedrock slopes with nearly uniform ~27° angles (Figure S2). The slope angle does not appear to be related to bedrock strength, as no evidence for slope failures is present. The possibility that these slopes are major fault scarps can be ruled out by our structural interpretation. Major erosional rills or gullies in these slopes are rare, occurring only around localized seeps and springs, and the slopes are very smooth overall, but small linear gullies and associated debris aprons are present (Figure S4b). Most of these slopes have not accumulated talus at the base, where bedrock is often exposed (Figure S4d).Others appear to have shed a thin layer of debris into the depression (contributing the terrace deposits described above). Because the slopes drain into a closed depression, wind erosion is likely required to explain the lack of colluvial and alluvial debris that would accumulate at the base. The rectilinear profile indicates that the slope retreat is weathering-limited, i.e., debris is removed faster than it can accumulate. Given the limited occurrence of major erosional features on the slopes, it is possible that some portions of them retreat mainly by eolian deflation aided by salt weathering, as proposed for rectilinear bedrock slopes in the Dry Valleys of Antarctica (Selby, 1971). Infrequent precipitation events may also be effective at transporting debris down-slope.

Zones of active of salt weathering, previously noted by Goudie and Wells (1995), were observed around the the SdF. Salt presently accumulates around the margins of modern pans, and evaporites evidently accumulate on subsurface discontinuities such as unconformities (Figures S5 and S6). Salt crusts are visible in aerial imagery in many locations around the margin of the SdF (Figures S4b, S4c, and S5). We observed tafoni on the windward face of an ignimbrite outcrop located downwind of an evaporite pan NW of the SdF (Figure S7). Given these observations, we infer that salt weathering in the SdF provides a means of breaking down Cenozoic bedrock into particles that can be more easily entrained by wind.

Near its western rim, the SdF hosts large, smooth, elongated ridges, 5–10 km in length and up to 600 m tall (Figure 3), elsewhere interpreted as fault scarps (Reijs and McClay, 2003). Cross section B (Figure 5), however, indicates that these ridges are erosional. They are not parallel to wind directions inferred from smaller-scale landforms, but their long axes generally parallel the strike of underlying strata. The ridges thus reflect the strong influence

©2020 American Geophysical Union. All rights reserved.

of bedding orientation and lithology superimposed on erosional processes in the SdF. Their dip slopes correspond to the upper Chacras Formation, a unit of relatively resistant cross-bedded sandstones and conglomerates that contrasts with overlying Potrero Grande volcaniclastics (Adelmann, 2001). We hypothesize that these resistant strata slowed the excavation of the depression, leading to elongated erosional remnants that parallel the strike of bedding planes; these topographic remnants were likely smoothed by weathering, colluvial transport, and eolian deflation.

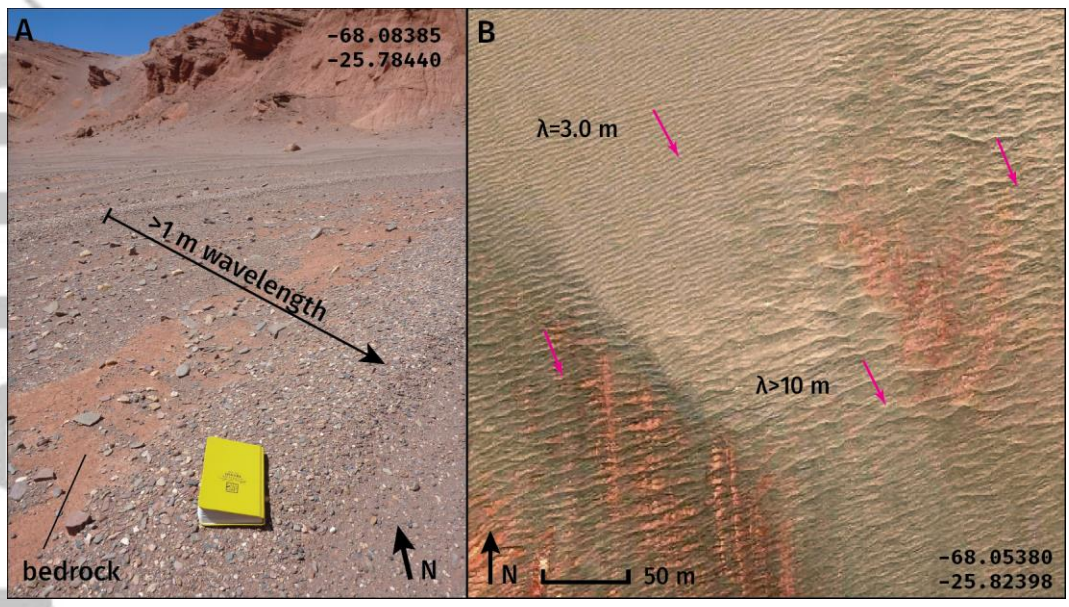

Figure 8. (**a**) Eolian megaripples photographed on a Permian bedrock surface in the Salina del Fraile. (**b**) Aerial imagery (Bing Maps) of eolian megaripples disrupting a stony lag deposit and exposing orange Quiñoas Formation bedrock. Refer to Figure 3 for the locations of images.

Five kilometers southeast of the SdF, three ~300 m tall mesas with smooth, linear slopes are present (Figures 3 and 6b). They are 5.5–10.5 km^2 in area with curvilinear planforms 2.5–6 km long that taper slightly to the SE. The tops of the mesas are subhorizontal and characterized by heavily abraded bedrock surfaces (Figure S3d). Although the mesas resemble alluvial terraces in some respects, no evidence of fluvial channels or paleochannels is present. Instead, they correlate with a regional, subhorizontal, Late Miocene–Pliocene surface representing the top of the Potrero Grande Formation and/or Late Miocene volcanic flows in this area (Richards et al., 2006) and are therefore composed of Potrero Grande volcaniclastics.

Although it is difficult to imagine how fluvial or tectonic processes could produce these mesas, our wind erosion hypothesis provides a potential explanation. The mesas are larger and smoother than megayardangs described in indurated ignimbrites nearby on the Puna Plateau and in Northern Chile (de Silva et al., 2010), but are similar in planform shape to megayardangs in Crommelin crater, Mars, that developed in canyon networks reworked by wind erosion (Perkins et al., 2015, and Figure 1b therein). As evidenced by the lack of boulder-sized colluvium, the lithologic composition of the smooth mesas is more friable than well-indurated ignimbrite and not capable of supporting the near-vertical slopes characteristic of some megayardangs (de Silva et al., 2010). The volcaniclastic sediments may also be more prone to disintegration by weathering and deflation. Like terrestrial megayardangs, the

©2020 American Geophysical Union. All rights reserved.

smooth mesas most likely result from a combination of processes, including colluvial and alluvial diffusion, but their overall forms are indicative of eolian streamlining and deflation.

The base of the smooth mesas corresponds to the contact between Potrero Grande Formation volcaniclastics and Chacras Formation conglomerates, an erodibility barrier, while the top of the mesas correlates to a regional subhorizontal surface composed of thin volcanic flows resting on top of the Potrero Grande Formation (Voss, 2002; Richards et al., 2006), which could act as a caprock. Mesa height (~300 m) is roughly equivalent to the thickness of the Potrero Grande Formation. The mesas are separated by smooth troughs elongated in the direction of the dominant wind direction. The troughs are floored by abraded bedrock surfaces, mostly composed of Chacras conglomerates, with meter-scale erosional and fault scarps (Figure S3d). The planform shape of the mesas is elongated and tapers slightly in the downwind direction, and their windward slopes appear to be smoothed and streamlined. The mesas are morphologically similar to streamlined hills and islands described in megaflood landscapes (e.g., Baker, 2009). Given the lack of evidence for megafloods in the study area, we suggest that the mesas formed by eolian downcutting into an erodible layer (Potrero Grande volcaniclastics) underlying a resistant caprock, a model similar to one proposed for the interior of Gale crater, Mars (Day and Kocurek, 2016).

The mesas are deformed by a swarm of penetrative normal faults with 400–800 m spacing that display smaller scarps in the troughs separating the mesas than on their top surfaces (Figure S3d). Twenty kilometers to the southwest, this fault swarm deforms volcanic flows dated to 3.61 Ma (Adelmann, 2001), indicating that a significant portion of the extensional deformation was accommodated by faulting after ~3.6 Ma. This timeframe agrees with the one we infer for wind erosion, suggesting that the smaller scarps observed in the troughs between the mesas is due to preferential erosion of the troughs during active faulting.

Predominant wind directions inferred from the long axes of yardangs, megaripple crests, and other landforms match closely with the downwind direction of strong winds obtained from the NASA MERRA reanalysis data (Figure 3, inset). Although the hourly MERRA data do not capture extreme wind gusts, which likely exceed 100 m/s in the southern Puna (Milana, 2009), they support the notion that these features result from strong, unidirectional, relatively infrequent winds. The data also suggest that the wind regime in the region has been stable throughout the late Quaternary and similar to the present, with strong winds directed toward the SE.

3.4 Timing and rate of erosion

Structural cross-sections, drawn conservatively to minimize the amount of erosion, show that up to 1,170 m and 1,950 m of strata were removed from the northern and central SdF, respectively (Figures 4 and 5). Existing chronostratigraphic ages provide constraints on the timing and rate of this erosion (Figure 9a). The initiation of erosion is bracketed by the top unit exposed in the depression, the Potrero Grande Formation, 17.0 Ma (Adelmann, 2001, K–Ar of biotite), and by the oldest volcanic ash deposited within the floor of the depression, 8.2 Ma (Voss, 2002, Ar–Ar of biotite). The depression therefore must have already been partially excavated by 8.2 Ma. Streamlining and erosion of terraces containing 2.6 Ma and 4.0 Ma ashes in the floor of the depression (Voss, 2002, Ar–Ar of plagioclase) also indicates significant erosion since the Pliocene. Yardangs and megaripples, active salt weathering zones, a lack of major sedimentary fill, rectilinear bedrock slopes, and imaged dust storms all indicate that erosion is currently active in the region (Goudie & Wells, 1995; Milana & Kröhling, 2017).

©2020 American Geophysical Union. All rights reserved.

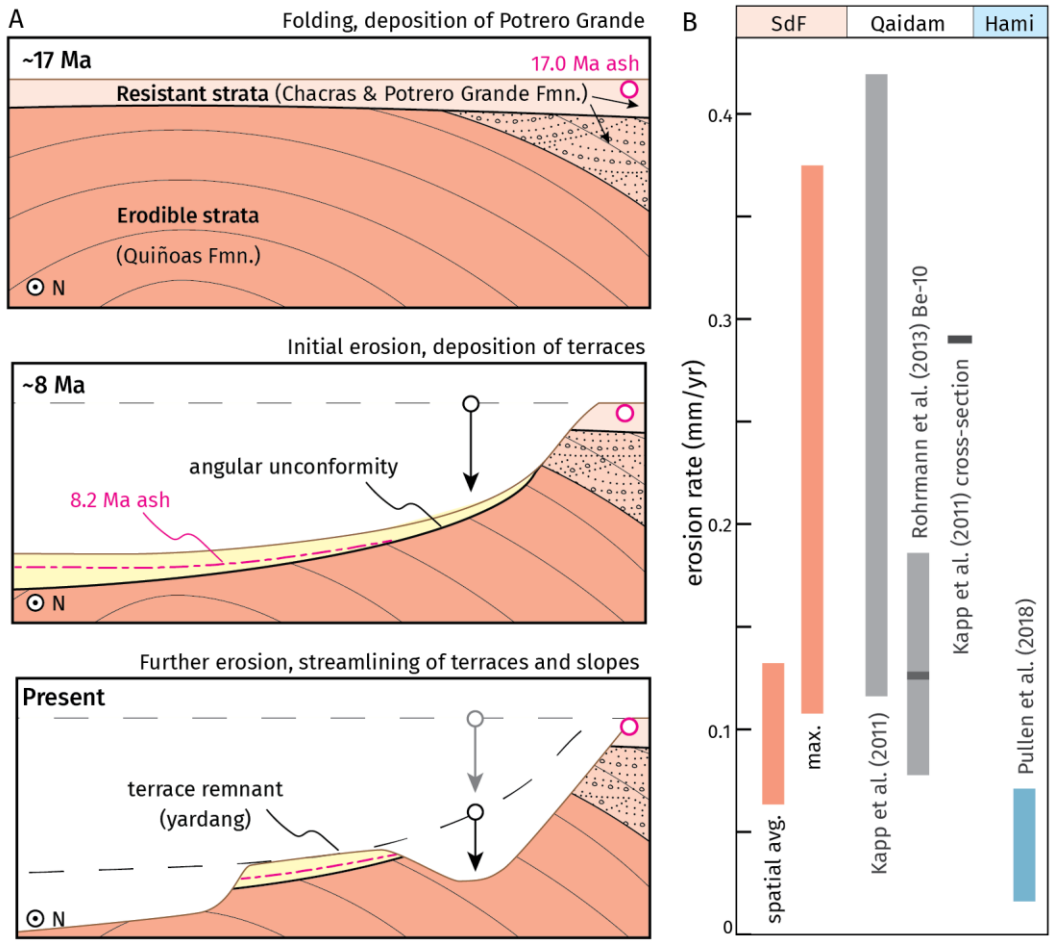

Figure 9. (**a**) Timing of wind erosion of the Salina del Fraile depression inferred from structural and chronostratigraphic data. (**b**) Comparison of erosion rates to previous studies of wind erosion in the Qaidam Basin, China (Kapp et al., 2011; Rohrmann et al., 2013) and the Hami Basin, China (Pullen et al., 2018).

Given that erosion began between 17 and 8.2 Ma and is presently ongoing, we estimate erosion rates using the structural cross-sections presented in Section 3.1. A maximum thickness of eroded material of 1.95 km measured from section B (Figure 5), yields maximum erosion rates of 0.11– 0.23 mm/yr in the central part of the depression. An average of 1.05 km of strata have been eroded from cross-sections A and B (Figures 4 and 5). Using this as a spatial average over the area of the basin floor, wind has removed ~315 km^3 of material from the depression since 17-8.2 Ma, averaging 0.062–0.13 mm/yr. Fluvial drainage networks (Figure S1) presently cover approximately 10% of the surface in the SdF. These erosion rates may overestimate the contribution of wind erosion of bedrock by up to 10%, but any fluvial sediment ultimately requires wind to be removed from the depression. While these estimates are long-term (~10^7 yr), they fall within the range of rates reported elsewhere for wind erosion over time scales of millions of years (Figure 9b) and are 2¬10 times lower than those calculated from cross-sections in the Qaidam basin, China, involving wind erosion of folded Pliocene strata (Kapp et al, 2011; Rohrmann et al., 2013). The spatially averaged erosion rate of ~0.06 mm/yr estimated here is very similar to the average erosion rate estimated for the Hami depression in northern China (Figure 9b), which involved

©2020 American Geophysical Union. All rights reserved.

deflation of Neogene strata containing conglomeratic and sandstone layers (Pullen et al., 2018).

3.5 Implications

The erosional origin of the Salina del Fraile depression has implications for the late Cenozoic tectonics of the Puna Plateau. Previous researchers suggested a Pliocene phase of orogen-parallel sinistral strike-slip kinematics based on the morphology of the depression, with up to 7.7 km of offset on a purported Salina del Fraile fault system (Reijs and McClay, 2003). Such an interpretation, however, challenges measurements of nearby fault kinematics that imply orogen-parallel dextral deformation during this time (Allmendinger et al., 1989; Kraemer et al., 1999; Zhou et al., 2015). Our inference that the depression is erosional obviates the need to invoke orogen-parallel sinistral tectonics and implies that Pliocene to Recent extensional deformation was accommodated by the normal faults apparent in Figure 3, which may be splays off the dextral Acazoque fault system that terminates near the Salar de Antofalla (Kraemer et al., 1999).

The initiation of wind erosion between 17 and 8.2 Ma is broadly consistent with a documented phase of aridification on the Puna Plateau partially driven by the uplift of ranges east of the study area (Strecker et al., 2007), such as the Sierra Laguna Blanca (exhumed 15–10 Ma; Zhou et al., 2017). Late Miocene aridification is also partially attributed to global cooling forced by a decline in atmospheric CO2 (Herbert et al., 2016). Global aridification and cooling during the Late Miocene is reflected in ocean temperature proxies and in various moisture and temperature proxies compiled throughout Eurasia (Miao et al., 2012). Large-scale eolian deflation and excavation of topographic depressions, such as the Salina del Fraile and the Hami basin in central Asia (Pullen et al., 2018) may represent a topographic signal of this episode of global climate change. Alternatively, existing data also permit the interpretation that erosion began as soon as the package of friable strata was tectonically deformed and exposed at ~17 Ma.

The idea that high-relief topography can be generated and sustained by eolian processes, with magnitudes of deflation up to 2 km, has implications for similar landforms on Earth and other planetary surfaces. The Central Andes hosts several depressions 10–50 km in width that, while little studied, may have been partially formed by wind erosion (Figure 1). Previous research indicates that the Purulla Basin (Figure 1, location B) may have experienced an average deflation of roughly ~4 m during the Holocene, approximately 0.3 mm/yr (Milana & Kröhling, 2017). Although more work should be done to quantify erosion rates in wind-dominated areas of the Puna, the Salina del Fraile suggests that the magnitude of eolian erosion throughout the Cenozoic may be significant in these internally drained regions lacking major fluvial incision.

Many martian landforms are thought to be formed by wind erosion over long timescales. Mounds of sedimentary strata located in the centers of impact craters preserve records of past climates and are important exploration targets (Anderson and Bell, 2010). A substantial amount of wind erosion (up to a few km) is necessary to form the present morphology of many central mounds, whether they are remnants of crater-filling material (Bennett and Bell, 2016; Steele et al., 2018), or they formed in-place (Kite et al., 2013). The lower flank of Mount Sharp, the central mound of Gale crater, consists of erosional buttes, mesas, and canyons that strongly resemble the smoothed mesas and elongated ridges described above (Figure 10).

©2020 American Geophysical Union. All rights reserved.

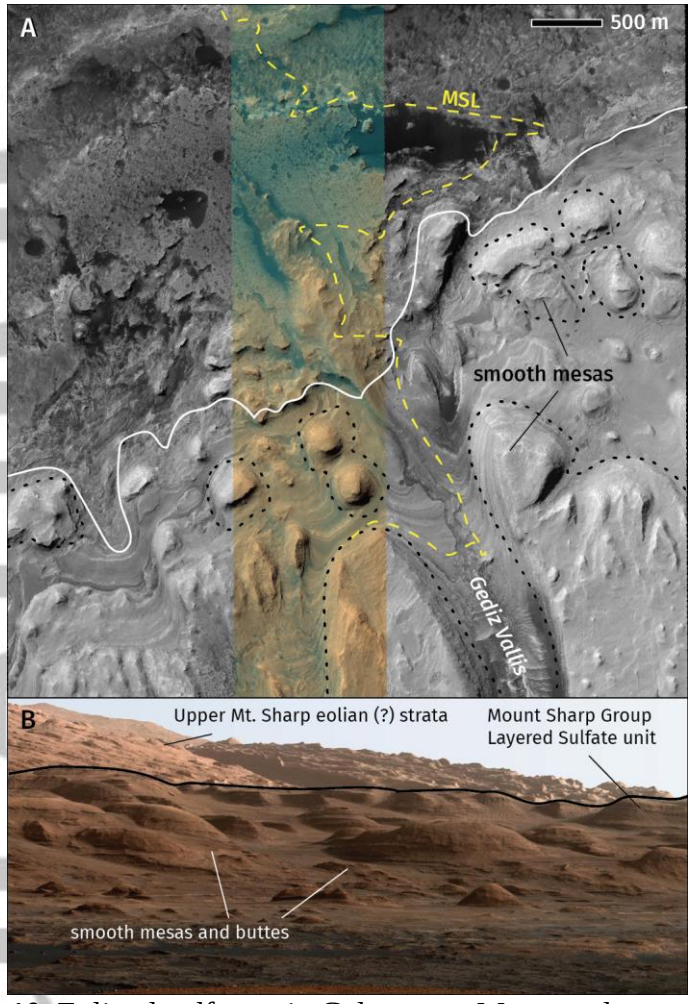

Figure 10. Eolian landforms in Gale crater, Mars, analogous to the smooth mesas near Salina del Fraile, Argentina. (**a**) Strata on the the NW flank of Mt. Sharp are eroded into streamlined mesas and buttes (indicated by black dotted lines) of the Layered Sulfate unit of the Mount Sharp Group (delineated by white line; stratigraphy of Fraeman et al., 2016). Yellow line approximates the planned path of the Mars Science Laboratory Curiosity rover (MSL). Cutout from MRO/HiRISE image ESP_061961_1750_MIRB (NASA/JPL/University of Arizona). The central ~1.2 km wide color band derives from merged infrared, red, and blue-green (IRB) channels, while the grayscale image derives only from the red channel. (**b**) Portion of white-balanced photomosaic of lower Mt. Sharp showing the profile of these streamlined erosional buttes and mesas. Acquired by Curiosity's Mast Camera (Mastcam) on September 20, 2012 (PIA16768; NASA/JPL-Caltech/MSSS).

Mudstones on the floor of Gale crater have exposure ages of only 78 ± 30 Ma, likely due to wind-driven bedrock scarp retreat (Farley et al., 2014). This relatively recent exposure increases the likelihood that complex organic molecules are preserved in near-surface materials. Identifying regions of rapid wind erosion is therefore critical for future missions exploring potentially habitable environments on Mars (Chojnacki et al., 2018). Like Gale and other martian craters including Jezero, the proposed landing site of the Perseverance rover, portions of the interior of the SdF are characterized by ongoing eolian erosion of lacustrine and alluvial strata that once partially filled the depression (Palucis et al., 2016; Chojnacki et al., 2018). The SdF thus represents a terrestrial analogue to martian landforms that are the target of exploratory missions.

©2020 American Geophysical Union. All rights reserved.

5 Conclusions

Structural and chronostratigraphic data show that the SdF depression was excavated by erosion of up to 2 km of friable, Paleogene strata exposed in compressional folds. Wind, rather than water or ice, was the dominant agent of erosion during at least the past 8.2 Ma. This inference is based on depositional ages of alluvial and lacustrine deposits contained within the depression, the prevalence of erosional eolian landforms within and around the depression, the lack of integrated fluvial networks, and the regional geomorphic context, which is presently dominated by wind erosion.

Inferred erosion rates of 0.06–0.23 mm/yr are typical of arid regions on Earth, but the large magnitude of erosion reflects the long time period (>8.2 Ma) during which eolian deflation took place. The SdF documents a Late Miocene to Quaternary source of eolian sand and dust in the southern Puna Plateau and exhibits some of the largest eolian landforms on Earth. In addition to the SdF depression itself, these include kilometer-scale elongated ridges and smoothed mesas resembling megayardangs and eolian landforms on Mars. Due to lithologic variation and tectonic folding, which produce erodibility contrasts, these high-relief landforms can be sustained without significant fluvial or glacial incision. Although the SdF is relatively well-studied, similar internally drained depressions in the Central Andes and other regions may also have been partially formed by wind erosion. Study of these landforms may yield insights into the evolution of Earth's arid regions on timescales of 10^6–10^7 yr, including how tectonic deformation and climate interact in such landscapes

Acknowledgments

The authors have no conflicts of interest to disclose. Support for this work was provided by an NSERC Discovery Grant and Discovery Accelerator Supplement to L. Schoenbohm. We thank Yanina Rojo and Santiago Uriburu Q. for assistance in the field, and we are grateful to Erin Seagren and Jeremy Rimando for helpful advice and discussions that strengthened the manuscript. We sincerely thank Jon Perkins, Paul Kapp, and an anonymous reviewer for helpful comments. Structural and geochronological data for this research are available in McMillan and Schoenbohm (2020) and online at https://doi.org/10.5683/SP2/UHDHGY. NASA MERRA data are available online at https://disc.gsfc.nasa.gov/.

References

Abell, J. T., Pullen, A., Lebo, Z. J., Kapp, P., Gloege, L., Metcalf, A. R., Nie, J., & Winckler, G. (2020). A wind-albedo-wind feedback driven by landscape evolution. *Nature Communications, 11,* 1–9. https://doi.org/10.1038/s41467-019-13661-w

Adelmann, D. (2001). Känozoische Beckenentwicklung des zentralandinen Puna-Plateaus (NW-Argentinien): Das Gebiet um den Salar de Antofalla und ein Vergleich zur nördlichen Puna, (Doctoral dissertation). Berlin: Freien Universität Berlin.

Allmendinger, R. W., Strecker, M., Eremchuk, J. E., & Francis, P. (1989). Neotectonic deformation of the southern Puna Plateau, northwestern Argentina. *Journal of South American Earth Sciences, 2,* 111–130. https://doi.org/10.1016/0895-9811(89)90040-0

Alonso, R. N., Jordan, T. E., Tabbutt, K. T. & Vandervoort, D. S. (1991). Giant evaporite belts of the Neogene central Andes. *Geology, 19,* 401–404.

Anderson. R. B., & Bell, J. F. III. (2010). Geologic mapping and characterization of Gale Crater and implications for its potential as a Mars Science Laboratory landing site. *Mars, 5,* 76–128. https://doi.org/10.1555/mars.2010.0004

©2020 American Geophysical Union. All rights reserved.

Aref, M. A. M., El-Khoriby, E., & Hamdan, M. A. (2002). The role of salt weathering in the origin of the Qattara Depression, Western Desert, Egypt. *Geomorphology, 45*(3-4), 181–195. https://doi.org/10.1016/S0169-555X(01)00152-0

Baker, V. R. (2009). The Channeled Scabland: A retrospective. *Annual Review of Earth and Planetary Sciences, 37*, 393–411. https://doi.org/10.1146/annurev.earth.061008.134726

Bennett, K. A., & Bell, J. F. III. (2016). A global survey of martian central mounds: Central mounds as remnants of previously more extensive large-scale sedimentary deposits. *Icarus, 264,* 331–341. https://doi.org/10.1016/j.icarus.2015.09.041

Bookhagen, B., & Strecker, M. R. (2008). Orographic barriers, high-resolution TRMM rainfall, and relief variations along the eastern Andes. Geophysical Research Letters, *35*, L06403. https://doi.org/10.1029/2007GL032011

Bridges, N. T., Spagnuolo, M. G., de Silva, S. L., Zimbelman, J. R., & Neely, E. M. (2015). Formation of gravel-mantled megaripples on Earth and Mars: Insights from the Argentinean Puna and wind tunnel experiments. *Aeolian Research,* 17, 49–60. https://doi.org/10.1016/j.aeolia.2015.01.007

Brock, E. J. & Twidale, C. R. (2011). J. T. Jutson and the work of the wind in shaping the landscape. *Geographical Research, 49,* 47–58. https://doi.org/10.1111/j.1745-5871.2010.00662.x

Canavan, R. R., Carrapa, B., Clementz, M. T., Quade, J., DeCelles, P. G., & Schoenbohm, L. M. (2014). Early Cenozoic uplift of the Puna plateau, Central Andes, based on stable isotope paleoaltimetry of hydrated volcanic glass. *Geology, 42*, 447–450. https://doi.org/10.1130/G35239.1

Carrapa, B., Adelmann, D., Hilley, G. E., Mortimer, E., Sobel, E. R., & Strecker, M. R. (2005). Oligocene range uplift and development of plateau morphology in the southern central Andes. *Tectonics, 24,* TC4011. https://doi.org/10.1029/2004TC001762

Chojnacki, M., Banks, M., & Urso, A. (2018). Wind-driven erosion and exposure potential at Mars 2020 rover candidate-landing sites. *Journal of Geophysical Research: Planets, 123*, 468–488. https://doi.org/10.1002/2017JE005460

Day, M., & Kocurek, G. (2016). Observations of an aeolian landscape: From surface to orbit in Gale Crater. *Icarus, 280,* 37–71. https://doi.org/10.1016/j.icarus.2015.09.042

DeCelles, P. G., Carrapa, B., Horton, B. K., McNabb, J., Gehrels, G. E., & Boyd, J. (2015). The Miocene Arizaro Basin, central Andean hinterland: Response to partial lithosphere removal? *Geological Society of America Memoirs, 212,* 359–386. https://doi.org/10.1130/2015.1212(18)

de Silva, S. L. (2010). The largest wind ripples on Earth: COMMENT. *Geology, 38,* e218. https://doi.org/10.1130/G30780C.1

de Silva, S. L., Bailey, J. E., Mandt, K. E., & Viramonte, J. M. (2010). Yardangs in terrestrial ignimbrites: Synergistic remote and field observations on Earth with applications to Mars. *Planetary and Space Science, 58,* 459–471. https://doi.org/10.1016/j.pss.2009.10.002

de Silva, S. L., Spagnuolo, M. G., Bridges, N. T., & Zimbelman, J. R. (2013). Gravel-mantled megaripples of the Argentinean Puna: A model for their origin and growth

©2020 American Geophysical Union. All rights reserved.

with implications for Mars. *Bulletin of the Geological Society of America*, *125*(11-12), 1912–1929. https://doi.org/10.1130/B30916.1

Farley, K. A. et al. (2014). In situ radiometric and exposure age dating of the Martian surface. *Science, 343,* 1247166. https://doi.org/10.1126/science.1247166

Fraeman, A. A., Ehlmann, B. L., Arvidson, R. E., Edwards, C. S., Grotzinger, J. P., Milliken, R. E., Quinn, D. P., & Rice, M. S. (2016). The stratigraphy and evolution of lower Mount Sharp from spectral, morphological, & thermophysical orbital data sets. *Journal of Geophysical Research: Planets*, *121*, 1713–1736. https://doi.org/10.1002/2016JE005095

Gaiero, D. M. (2007). Dust provenance in Antarctic ice during glacial periods: From where in southern South America? *Geophysical Research Letters*, *34*, L17707. doi:10.1029/2007GL030520.

Goudie, A. S. (2007). Mega-yardangs: A global analysis. *Geography Compass*, *1,* 65–81. https://doi.org/10.1111/j.1749-8198.2006.00003.x

Goudie, A. S. (2012). Charles Rollin Keyes and extravagant aeolation. *Aeolian Research, 4,* 51–53. https://doi.org/10.1016/j.aeolia.2012.01

Goudie, A. S. (2018). Dust storms and ephemeral lakes. *Desert*, *23*(1), 153–164. https://doi.org/10.22059/jdesert.2018.66370

Goudie, A. S., & Day, M. J. (1980). Disintegration of fan sediments in Death Valley, California, by salt weathering. *Physical Geography*, *1*(2), 126–137. https://doi.org/10.1080/02723646.1980.10642195

Goudie, A. S., & Wells, G. L. (1995). The nature, distribution and formation of pans in arid zones. *Earth Science Reviews, 38,* 1–69. https://doi.org/10.1016/0012-8252(94)00066-6

Haselton, K., Hilley, G., & Strecker, M. R. (2002). Average Pleistocene climatic patterns in the southern central Andes: Controls on mountain glaciation and paleoclimate implications. *Journal of Geology*, *110,* 211–226. https://doi.org/10.1086/338414

Herbert, T. D., Lawrence, K. T., Tzanova, A., Peterson, L. C., Caballero-Gill, R., & Kelly, C. S. (2016). Late Miocene global cooling and the rise of modern ecosystems. *Nature Geoscience, 9,* 843–847. https://doi.org/10.1038/ngeo2813

Hermanns, R. L., Niedermann, S., Villanueva Garcia, A., Gomez, J. S., & Strecker, M. R. (2001). Neotectonics and catastrophic failure of mountain fronts in the southern intra-Andean Puna Plateau, Argentina. *Geology*, *29,* 619–623. https://doi.org/10.1130/0091-7613(2001)029<0619:NACFOM>2.0.CO;2

Hugenholtz, C. H., Barchyn, T. E., & Favaro, E. A. (2015). Formation of periodic bedrock ridges on Earth. *Aeolian Research, 18,* 135–144. https://doi.org/10.1016/j.aeolia.2015.07.002

Isla, F. & Espinosa, M. (2017). Upper Quaternary evolution of the dune field of the Bolsón de Fiambalá, Catamarca: Sand dispersal at the Andes piedmonts. *Quaternary International, 442,* 59–66. https://doi.org/10.1016/j.quaint.2016.07.037

Kapp, P., Pelletier, J. D., Rohrmann, A., Heermance, R., Russell, J., & Ding, L. (2011). Wind erosion in the Qaidam basin, central Asia: Implications for tectonics, paleoclimate, and the source of the Loess Plateau. *GSA Today, 21*, 4–10. https://doi.org/10.1130/GSATG99A.1

©2020 American Geophysical Union. All rights reserved.

Kite, E. S., Lewis, K. W., Lamb, M. P., Newman, C. E., & Richardson, M. I. (2013). Growth and form of the mound in Gale Crater, Mars: Slope wind enhanced erosion and transport. *Geology, 41,* 543–546. https://doi.org/10.1130/G33909.1

Kraemer, B., Adelmann, D., Alten, M., Schnurr, W., Erpenstein, K., Kiefer, E., van den Bogaard, P., & Görler, K. (1999). Incorporation of the Paleogene foreland into the Neogene Puna plateau: The Salar de Antofalla area, NW Argentina. *Journal of South American Earth Sciences, 12,* 157–182. https://doi.org/10.1016/S0895-9811(99)00012-7

Lämmel, M., Meiwald, A., Yizhaq, H., Tsoar, H., Katra, I., & Kroy, K. (2018). Aeolian sand sorting and megaripple formation. *Nature Physics, 14,* 759–765. https://doi.org/10.1038/s41567-018-0106-z

McMillan, M & Schoenbohm, L. M. (2020). Large-Scale Cenozoic Wind Erosion in the Puna Plateau, *Scholars Portal Dataverse*, V1, UNF:6:IYumHRpsKMuN/fEcJ4fjWQ== [fileUNF]. https://doi.org/10.5683/SP2/UHDHGY

Miao, Y., Herrmann, M., Wu, F., Yan, X., & Yang, S. (2012). What controlled Mid-Late Miocene long-term aridification in Central Asia? - Global cooling or Tibetan Plateau uplift: A review. *Earth-Science Reviews, 112,* 155–172, https://doi.org/10.1016/j.earscirev.2012.02.003

Milana, J. P. (2009). Largest wind ripples on Earth?. *Geology, 37,* 343–346. https://doi.org/10.1130/G25382A.1

Milana, J. P. & Kröhling, D. M. (2017). First data on volume and type of deflated sediment from Southern Puna Plateau and its role as source of the Chaco-Pampean loess. *Quaternary International, 438,* 126–140. https://doi.org/10.1016/j.quaint.2017.03.007

Palucis, M. C., Dietrich, W. E., Williams, R. M. E., Hayes, A. G., Parker, T., Sumner, D. Y., Mangold, N., Lewis, K., & Newsom, H. (2016). Sequence and relative timing of large lakes in Gale crater (Mars) after the formation of Mount Sharp. *Journal of Geophysical Research: Planets, 121,* 472–496. https://doi.org/10.1002/2015JE004905

Pelletier, J. D., Kapp, P. A., Abell, J., Field, J. P., Williams, Z. C., & Dorsey, R. J. (2018). Controls on yardang development and morphology: 1. Field observations and measurements at Ocotillo Wells, California. *Journal of Geophysical Research*: *Earth Surface, 123,* 694–722. https://doi.org/10.1002/2017JF004461

Perkins, J. P., Finnegan, N. J., & de Silva, S. L. (2015). Amplification of bedrock canyon incision by wind. *Nature Geoscience, 8,* 305–310. https://doi.org/10.1038/ngeo2381

Perkins, J. P., Finnegan, N. J., de Silva, S. L., & Willis, M. J. (2019). Controls on eolian landscape evolution in fractured bedrock. *Geophysical Research Letters, 46*(21), 12012–12020. https://doi.org/10.1029/2019GL083955

Plakht, J., Patyk-Kara, N., & Gorellkova, N. (2000). Terrace pediments in Makhtesh Ramon, Central Negev, Israel. *Earth Surface Processes and Landforms*, *25*(1), 29–39. https://doi.org/10.1002/(SICI)1096-9837(200001)25:1<29::AID-ESP44>3.0.CO;2-D

Pullen, A., Kapp, P., & Chen, N. (2018). Development of stratigraphically controlled, eolian-modified unconsolidated gravel surfaces and yardang fields in the wind-eroded Hami Basin, northwestern China, Geological Society of America Bulletin, *130,* 630–648. https://doi.org/10.1130/B31734.1

©2020 American Geophysical Union. All rights reserved.

Quade, J., Dettinger, M. P., Carrapa, B., DeCelles, P. G., Murray, K. E., Huntington, K. W., Cartwright, A., Canavan, R. R., Gehrels, G., & Clementz, M. (2015). The growth of the central Andes, 22° S-26° S., in DeCelles, P. G., Ducea, M. N., Carrapa, B., & Kapp, P. A., eds., Geodynamics of a Cordilleran Orogenic System: The Central Andes of Argentina and Northern Chile. *Geological Society of America Memoir 212,* 277–308. https://doi.org/10.1130/2015.1212(15)

Reijs, J., & McClay, K. (2003). The Salina del Fraile pull-apart basin, northwest Argentina. In Storti, F., Holdsworth, R. E., & Salvini, F. (Eds.), *Intraplate Strike-Slip Deformation Belts, Special Publication Series* (Vol. 210, pp. 197–209). London: The Geological Society of London. https://doi.org/10.1144/Gsl.Sp.2003.210.01.12

Richards, J. P., Ullrich, T., & Kerrich, R. (2006). The Late Miocene-Quaternary Antofalla volcanic complex, southern Puna, NW Argentina: Protracted history, diverse petrology, and economic potential. *Journal of Volcanology and Geothermal Research, 152,* 197–239. https://doi.org/10.1016/j.jvolgeores.2005.10.006

Rohrmann, A., Heermance, R., Kapp, P., & Cai, F. (2013). Wind as the primary driver of erosion in the Qaidam Basin, China. *Earth and Planetary Science Letters, 374,* 1–10. https://doi.org/10.1016/j.epsl.2013.03.011

Schwanghart, W., & Scherler, D. (2014). TopoToolbox 2 – MATLAB-based software for topographic analysis and modeling in Earth surface sciences. *Earth Surface Dynamics, 2,* 1–7. https://doi.org/10.5194/esurf-2-1-2014

Seggiaro, R., Becchio, R., Pereyra, F., & Martínez, L. (2007). *Hoja Geológica 2569-IV, Antofalla, provincias de Catamarca y Salta* (Boletín 343, scale 1:250,000). Buenos Aires: Instituto de Geología y Recursos Minerales, Servicio Geológico Minero Argentina, Programa Nacional de Cartas Geológicas. https://repositorio.segemar.gob.ar/handle/308849217/97

Selby, M. J. (1971). Slopes and their development in an ice-free, arid area of Antarctica: *Geografiska Annaler: Series A, Physical Geography, 53,* 235–245. https://doi.org/10.1080/04353676.1971.11879849

Steele, L. J., Kite, E. S., & Michaels, T. I. (2018). Crater mound formation by wind erosion on Mars. *Journal of Geophysical Research: Planets, 123,* 113–130. https://doi.org/10.1002/2017JE005459

Strecker, M. R., Alonso, R. N., Bookhagen, B., Carrapa, B., Hilley, G. E., Sobel, E. R., & Trauth, M. H. (2007). Tectonics and climate of the southern Central Andes. *Annual Review of Earth and Planetary Sciences, 35,* 747–787. https://doi.org/10.1146/annurev.earth.35.031306.140158

Voss, R. (2002). Cenozoic stratigraphy of the southern Salar de Antofalla region, northwestern Argentina. *Andean Geology, 29,* 167–189. https://doi.org/10.4067/S0716-02082002000200002

Xiao, L., Wang, J., Dang, Y., Cheng, Z., Huang, T.,Zhao, J., Xu, Y., Huang, J., Xiao, Z., & Komatsu, G. (2017). A new terrestrial analogue site for Mars research: The Qaidam Basin, Tibetan Plateau (NW China). *Earth-Science Reviews, 164,* 84–101. https://doi.org/10.1016/j.earscirev.2016.11.003

Zhou, R., Schoenbohm, L. M., & Cosca, M. (2015). Recent, slow normal and strike-slip faulting in the Pasto Ventura region of the southern Puna Plateau, NW Argentina. *Tectonics, 32,* 19–33. https://doi.org/10.1029/2012TC003189

©2020 American Geophysical Union. All rights reserved.

Zhou, R., Schoenbohm, L. M., Sobel, E. R., Davis, D. W., & Glodny, J. (2017). New constraints on orogenic models of the southern Central Andean Plateau: Cenozoic basin evolution and bedrock exhumation. *Geological Society of America Bulletin, 129*, 152–170. https://doi.org/10.1130/B31384.1

Accepted Article

©2020 American Geophysical Union. All rights reserved.